

On local tracking algorithms for the simulation of three-dimensional discontinuities

Philippe Jäger · Paul Steinmann · Ellen Kuhl

Received: 4 June 2007 / Accepted: 20 January 2008 / Published online: 22 February 2008
© Springer-Verlag 2008

Abstract The present manuscript focuses on the algorithmic treatment of three-dimensional discontinuities within a purely displacement based finite element setting. In contrast to two-dimensional cracks, the local element based geometric representation of three-dimensional crack surfaces is non-unique and thus not straightforward. Accordingly, we compare different crack tracking strategies, one being algorithmically extremely efficient but yet somehow restrictive, the other one being more complex but rather general in nature. While the first method is able to represent entirely smooth discontinuity surfaces, the second approach introduces inter-element discontinuities in the overall crack surface representation. Both methods are compared systematically and additional comments about the algorithmic realization are provided. From the numerical results we conclude that neither of the two algorithms is able to solve all defined quality criteria satisfactorily, although both are mesh independent, computationally cheap and rather efficient. The ultimate solution might be an overall global crack surface representation that a priori circumvents a number of algo-

rithmic deficiencies and at the same time provides a unique and smooth three-dimensional crack surface representation.

Keywords Strong discontinuities · 3D crack propagation · Tracking algorithm · Cohesive law

1 Introduction

Within the past decade, the extended finite element method first introduced by Belytschko and co-workers [3,4] has advanced to a widely-accepted canonical technology to simulate propagating discontinuities within a finite element setting, see also [6,7,24,27,28]. In contrast to the classical extended finite element method which is based on the finite element discretization of displacements and displacement jumps, the recently introduced reparametrization by Hansbo et al. [12,13] is conveniently restricted to a purely displacement based finite element discretization, see also [2,14,16–18].

While both techniques are quite well-established in the context of two-dimensional crack propagation, their extension to three-dimensional crack phenomena is unfortunately not straightforward and we feel that some of the underlying computational issues deserve additional attention. First attempts along these lines have been made by Belytschko et al. [1] and Sukumar et al. [25] and significant recent progress has been documented by Gasser and Holzapfel [8,9]. When rising the number of spatial dimensions from two to three, most algorithmic changes are of minor concern, e.g., crack initiation and crack propagation criteria which are formulated in a general tensorial framework can easily be transformed into three dimensions. However, some technical implementational details still remain. For example, a discontinuity would always divide a two dimensional triangular element into one triangle and one quadrilateral element. Three dimensional

P. Jäger
Department of Mechanical Engineering,
University of Kaiserslautern, 67653 Kaiserslautern, Germany

P. Steinmann (✉)
Department of Mechanical Engineering,
Friedrich-Alexander University Erlangen-Nuremberg,
91058 Erlangen, Germany
e-mail: ps@rhrk.uni-kl.de

E. Kuhl
Department of Mechanical Engineering,
Stanford University, Stanford, CA 94305-4040, USA

E. Kuhl
Department of Bioengineering,
Stanford University, Stanford, CA 94305-4040, USA

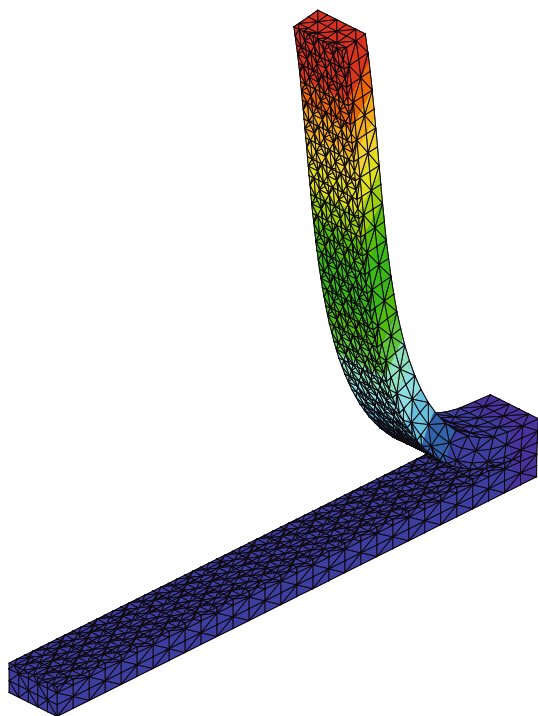


Fig. 1 Non-symmetric peel test. Simulation of bi-material layer with predefined crack plane normal discretized with 3,750 purely displacement based Hansbo discontinuity elements

tetrahedral, however, can be divided in two different ways introducing either a tetrahedron and a wedge element or two wedge elements, see [8, 19].

The most cumbersome issue related to three-dimensional discontinuities is probably the choice of an appropriate crack tracking algorithm. Most of the existing literature on three dimensional discontinuities including our own work is thus restricted to problems for which the discontinuity surface is a priori known. A typical problem along these lines is the classical peel test. Although the crack plane normal might undergo severe rotations for the non-symmetric peeling of a bi-material interface as displayed in Fig. 1, the normal vector can still be conveniently prescribed in the undeformed reference configuration. Knowing the crack plane normal a priori simplifies the algorithmic treatment to a large extent. For most technically relevant examples, however, the direction of the crack is initially unknown and a successful crack propagation simulation in three dimensions is impossible without identifying appropriate crack tracking strategies. Existing crack tracking algorithms can basically be classified in two categories, local and global tracking methods. The latter which are obviously more demanding from an algorithmic point of view are addressed in the recent work by Chaves [5], Oliver et al. [21, 22] and Jäger et al. [14].

Nevertheless, in this paper, we focus on the former class of methods, since they typically provide a highly efficient solu-

tion at relatively low computational cost. In particular, we aim at comparing two different local crack tracking methods, one initially introduced by the Belytschko group [10, 11, 26] and an alternative one by the Holzapfel group [8, 9]. As we will show, the Belytschko method essentially produces smooth discontinuity surfaces. It is extremely efficient, since algorithmic modifications are restricted to the element level. Unfortunately, it is limited to a particular subset of problems for which the direction of the crack path is not allowed to change drastically from one element to the other. These more complex phenomena are captured nicely by the Holzapfel method. This strategy is somewhat non-local since it relies on a global averaging of the crack path. Accordingly, algorithmic modifications beyond the element level cannot be avoided. Apart from its algorithmic complexity, the Holzapfel method suffers the essential drawback of non-smooth discontinuity surfaces. Due to the non-local averaging of crack plane normals, the crack surface might eventually exhibit jumps across the inter-element boundaries. When systematically elaborating different crack tracking algorithms, our group has thus come to the conclusion, that ultimately, an overall global crack representation might indeed be the only way to accurately eliminate all shortcomings of the currently available local crack tracking algorithms. Based on global averaging techniques, the Holzapfel method presents a first promising step in this direction.

This paper is organized as follows. After a short review of the governing equations in Sect. 2, we briefly discuss the finite element discretization within the framework of a purely displacement based Hansbo interpolation scheme in Sect. 3. We also address the issues of consistent linearization and provide the overall tangent stiffness matrix for the numerical implementation. Section 4 is the key section of this paper; it introduces different algorithms for crack initiation, crack propagation and crack tracking. In particular the latter is elaborated in terms of two alternative strategies which are then compared by means of numerical examples in Sect. 5. Finally, Sect. 6 concludes with a critical discussion of alternative local crack tracking procedures and identifies the need for algorithmically challenging global crack tracking strategies.

2 Governing equations

To set the stage and introduce our notation, we briefly reiterate the continuous boundary value problem of a three-dimensional body crossed by an arbitrary discontinuity.

2.1 Kinematic equations

The first step to incorporate discontinuities in the displacement field is to define the relevant kinematic quantities. In the present notation we define the reference configuration of

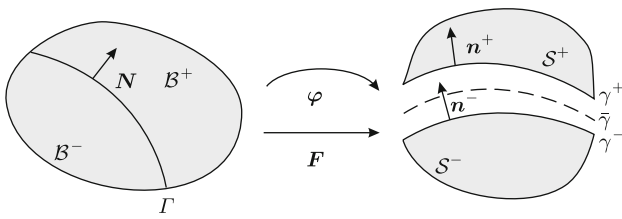


Fig. 2 Kinematics of non-linear deformation map

a body as \mathcal{B} with its positions \mathbf{X} and the spatial configuration as \mathcal{S} with its positions \mathbf{x} , see Fig. 2. If \mathcal{B} is crossed by a discontinuity Γ we divide the body \mathcal{B} into disjoint parts \mathcal{B}^+ and \mathcal{B}^- to ensure a unique non-linear deformation φ from the referential to the spatial configuration for each of the two parts.

$$\varphi(\mathbf{X}) := \begin{cases} \varphi^+(\mathbf{X}) & \forall \mathbf{X} \in \mathcal{B}^+ \\ \varphi^-(\mathbf{X}) & \forall \mathbf{X} \in \mathcal{B}^- \end{cases} \quad (1)$$

This deformation map is continuous in both parts of the body but can be discontinuous along the internal boundary Γ . Accordingly, the jump in the displacement field arises automatically as the difference of the deformation maps evaluated on both sides of the discontinuity.

$$[[\varphi]] = \varphi^+_{|\Gamma} - \varphi^-_{|\Gamma} \quad \forall \mathbf{X} \in \Gamma \quad (2)$$

As a result of the definition of the deformation map (1) all related kinematic quantities, the deformation gradient \mathbf{F} , its determinant J and all related stress and strain measures are defined independently on both sides \mathcal{B}^+ and \mathcal{B}^- as

$$\mathbf{F} = \begin{cases} \mathbf{F}^+ = \nabla_{\mathbf{X}} \varphi^+ & \forall \mathbf{X} \in \mathcal{B}^+ \\ \mathbf{F}^- = \nabla_{\mathbf{X}} \varphi^- & \forall \mathbf{X} \in \mathcal{B}^- \end{cases} \quad (3)$$

with $J^+ = \det(\mathbf{F}^+)$ and $J^- = \det(\mathbf{F}^-)$. Recall that due to the definition of the deformation map the one unique surface Γ is mapped onto two surfaces γ^+ and γ^- . We thus define a fictitious discontinuity surface $\bar{\gamma}$ which is centered in the spatial configuration, compare Fig. 3.

$$\bar{\varphi} := \frac{1}{2} [\varphi^+_{|\Gamma} + \varphi^-_{|\Gamma}] \quad \forall \mathbf{X} \in \Gamma \quad (4)$$

To complete the set of kinematic equations, we introduce all related average quantities, i.e., the deformation gradient $\bar{\mathbf{F}} = \frac{1}{2}[\mathbf{F}^+ + \mathbf{F}^-]$, the Jacobian $\bar{J} = \det \bar{\mathbf{F}}$ and the normal vector $\bar{\mathbf{n}} = \bar{J} \bar{\mathbf{F}}^{-t} \cdot \mathbf{N}$ on the fictitious surface $\bar{\gamma}$.

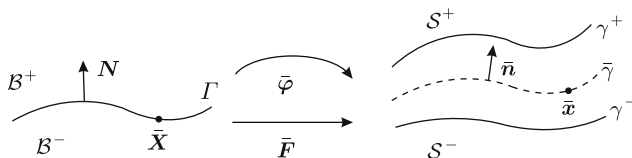


Fig. 3 Kinematics of fictitious discontinuity surface

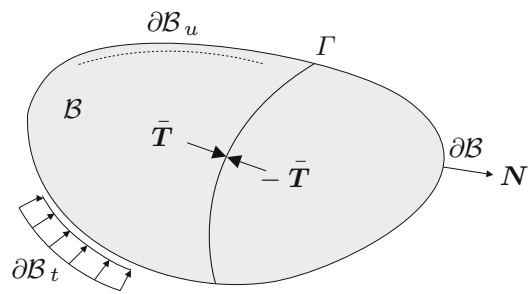


Fig. 4 Boundary value problem for cracked configuration

2.2 Equilibrium equations

Let the boundary $\partial\mathcal{B}$ in the referential configuration be subdivided into disjoint parts $\partial\mathcal{B} = \partial\mathcal{B}_u \cup \partial\mathcal{B}_t$ with $\partial\mathcal{B}_u \cap \partial\mathcal{B}_t = \emptyset$, where either Dirichlet or Neumann boundary conditions are prescribed. Along the fictitious surface Γ we require traction continuity in terms of the cohesive tractions $\bar{\mathbf{T}}$ for which we will introduce a constitutive law in Sect. 2.3. The boundary value problem of a cracked body \mathcal{B} can then be expressed through the following set of governing equations, here denoted in the reference configuration,

$$\begin{aligned} \text{Div } \mathbf{P} &= \mathbf{0} & \forall \mathbf{X} \in \mathcal{B}^+ \cup \mathcal{B}^- \\ \varphi &= \varphi^p & \forall \mathbf{X} \in \partial\mathcal{B}_u \\ \mathbf{P} \cdot \mathbf{N} &= \mathbf{T}^p & \forall \mathbf{X} \in \partial\mathcal{B}_t \\ \mathbf{P}^+ \cdot \mathbf{N} &= \mathbf{P}^- \cdot \mathbf{N} = \bar{\mathbf{T}} & \forall \mathbf{X} \in \Gamma \end{aligned} \quad (5)$$

where \mathbf{P} is the Piola stress. In the following we transfer the strong form of the boundary value problem (5.1), (5.3) and (5.4) into its weak form. By multiplication with a test function $\delta\varphi$ and integration by parts we obtain the corresponding integral format of the boundary value problem in the reference configuration.

$$\int_{\mathcal{B}^+ \cup \mathcal{B}^-} \delta \mathbf{F} : \mathbf{P} \, dV + \int_{\Gamma} [[\delta\varphi]] \cdot \bar{\mathbf{T}} \, dA = \int_{\partial\mathcal{B}_t} \delta\varphi \cdot \mathbf{T}^p \, dA \quad (6)$$

To express the above equation in terms of the symmetric Cauchy stress σ and the Cauchy tractions \mathbf{t}^p we perform a push forward to the spatial configuration.

$$\int_{\mathcal{S}^+ \cup \mathcal{S}^-} \nabla_{\mathbf{x}} \delta\varphi : \sigma \, dv + \int_{\bar{\gamma}} [[\delta\varphi]] \cdot \bar{\mathbf{t}} \, da = \int_{\partial\mathcal{S}_t} \delta\varphi \cdot \mathbf{t}^p \, da \quad (7)$$

2.3 Constitutive equations

In this subsection we specify the constitutive equations for the Cauchy stress σ inside the body and the cohesive Cauchy tractions $\bar{\mathbf{t}}$ along the discontinuity. The constitutive equations for the bulk stress σ are assumed to be of compressible Neo-Hooke type whereby σ can generally take different values on both sides of the discontinuity. The strain energy

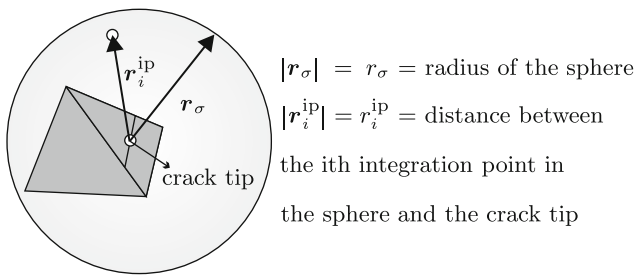


Fig. 5 Stress averaging sphere around the crack tip element introducing the set \mathcal{T}^σ of n^σ integration points within the sphere

function Ψ and the related stress measures \mathbf{P} and $\boldsymbol{\sigma}$ can be written in the following compact form,

$$\begin{aligned} \Psi &= \frac{1}{2}\mu [(\mathbf{F} \cdot \mathbf{F}^t) : \mathbf{I} - 3] - \mu \ln(J) + \frac{1}{2}\lambda \ln^2(J) \\ \mathbf{P} &= \frac{\partial \Psi}{\partial \mathbf{F}} = [\lambda \ln(J) - \mu \mathbf{F}^{-t} + \mu \mathbf{F}] \\ \boldsymbol{\sigma} &= \frac{1}{J} \mathbf{P} \cdot \mathbf{F}^t = \frac{1}{J} [\lambda \ln(J)\mathbf{I} - \mu \mathbf{I} + \mu \mathbf{F} \cdot \mathbf{F}^t] \end{aligned} \tag{8}$$

with λ and μ denoting the Lamé parameters. The inelastic behavior is attributed exclusively to the fictitious discontinuity surface through the cohesive crack concept, for which all inelastic deformations around the crack tip are collectively represented through the traction forces on the discontinuity, see, e.g., [6,7,24,27]. We assume an uncoupled traction separation law for which the normal traction vector $\bar{\mathbf{t}}_n$ is expressed exclusively in terms of the normal jump vector $\llbracket \boldsymbol{\varphi}_n \rrbracket = \llbracket \llbracket \boldsymbol{\varphi} \rrbracket \cdot \bar{\mathbf{n}} \rrbracket \bar{\mathbf{n}}$ and the in-plane traction vector $\bar{\mathbf{t}}_m$ is only a function of the tangential jump $\llbracket \boldsymbol{\varphi}_m \rrbracket = \llbracket \boldsymbol{\varphi} \rrbracket - \llbracket \boldsymbol{\varphi}_n \rrbracket$.

$$\bar{\mathbf{t}} = \begin{bmatrix} \bar{\mathbf{t}}_n \\ \bar{\mathbf{t}}_m \end{bmatrix} = \begin{bmatrix} f_t \exp\left(-\frac{f_t}{G_f} \llbracket \boldsymbol{\varphi}_n \rrbracket\right) \bar{\mathbf{n}} \\ d \llbracket \boldsymbol{\varphi}_m \rrbracket \end{bmatrix} \tag{9}$$

Here f_t denotes the tensile strength, G_f is the fracture energy and d is the shear stiffness.

3 Discretization

For the finite element formulation it proves convenient to distinguish between standard continuous elements and discontinuous elements which are crossed by the discontinuity surface. For the continuous elements, we apply a bilinear isoparametric interpolation leading to the following discretized sets of the node point coordinates \mathbf{X} , the displacement field $\boldsymbol{\varphi}$, the test functions $\delta\boldsymbol{\varphi}$ and their gradients \mathbf{F} and $\delta\mathbf{F}$.

$$\begin{aligned} \mathbf{X}|_{\mathcal{B}_e} &= \sum_{i=1}^{n_{en}} N^i \mathbf{X}_i \\ \boldsymbol{\varphi}|_{\mathcal{B}_e} &= \sum_{i=1}^{n_{en}} N^i \boldsymbol{\varphi}_i & \delta\boldsymbol{\varphi}|_{\mathcal{B}_e} &= \sum_{i=1}^{n_{en}} N^i \delta\boldsymbol{\varphi}_i \\ \mathbf{F}|_{\mathcal{B}_e} &= \sum_{i=1}^{n_{en}} \boldsymbol{\varphi}_i \otimes \nabla_X N^i & \delta\mathbf{F}|_{\mathcal{B}_e} &= \sum_{i=1}^{n_{en}} \delta\boldsymbol{\varphi}_i \otimes \nabla_X N^i \end{aligned} \tag{10}$$

Here N_i are the standard shape functions for tetrahedral elements and n_{en} is the number of element nodes. Theoretically, for the discontinuous elements, the displacement field $\boldsymbol{\varphi}^{(+,-)}$ and its gradient $\mathbf{F}^{(+,-)}$ are only defined in the corresponding part $\mathcal{B}^{(+,-)}$. Computationally, however, they are interpolated over the entire element through the nodal values in terms of the standard basis functions N^i . We therefore introduce two copies of the standard basis functions with n_{en}^+ nodes for the interpolation on one side of the discontinuity and n_{en}^- nodes for the other side. Technically speaking, the interpolated fields are set to zero on one side of the discontinuity, while they take their usual values on the other side. Accordingly, the jumps in the displacement field (2) and in the test function can then be expressed as the difference of the two continuous fields evaluated at the internal boundary Γ .

$$\begin{aligned} \llbracket \boldsymbol{\varphi} \rrbracket|_\Gamma &= \sum_{i=1}^{n_{en}^+} N^i|_\Gamma \boldsymbol{\varphi}_i^+ - \sum_{i=1}^{n_{en}^-} N^i|_\Gamma \boldsymbol{\varphi}_i^- = \sum_{i=1}^{n_{en}^+ + n_{en}^-} \bar{N}^i \boldsymbol{\varphi}_i \\ \llbracket \delta\boldsymbol{\varphi} \rrbracket|_\Gamma &= \sum_{i=1}^{n_{en}^+} N^i|_\Gamma \delta\boldsymbol{\varphi}_i^+ - \sum_{i=1}^{n_{en}^-} N^i|_\Gamma \delta\boldsymbol{\varphi}_i^- = \sum_{i=1}^{n_{en}^+ + n_{en}^-} \bar{N}^i \delta\boldsymbol{\varphi}_i \end{aligned} \tag{11}$$

Here the newly introduced sets \bar{N} consist of the element shape functions \bar{N} evaluated at Γ multiplied by the corresponding algebraic sign. Finally we discretize the average deformation gradient $\bar{\mathbf{F}}$

$$\begin{aligned} \bar{\mathbf{F}}|_\Gamma &= \frac{1}{2} \left[\sum_{i=1}^{n_{en}^+} \boldsymbol{\varphi}_i^+ \otimes \nabla_X N^i|_\Gamma + \sum_{i=1}^{n_{en}^-} \boldsymbol{\varphi}_i^- \otimes \nabla_X N^i|_\Gamma \right] \\ &= \sum_{i=1}^{n_{en}^+ + n_{en}^-} \boldsymbol{\varphi}_i \otimes \nabla_X \bar{N}^i \end{aligned} \tag{12}$$

With the help of the above introduced discretizations, the weak form of the governing equations (7) can be cast into the following discrete residual statement

$$\mathbf{R}_I = \mathbf{R}_I^{\text{int}} + \mathbf{R}_I^{\text{coh}} - \mathbf{R}_I^{\text{ext}} = \mathbf{0} \tag{13}$$

in terms of internal, cohesive and external contributions.

$$\begin{aligned} \mathbf{R}_I^{\text{int}} &= \mathbf{A}_{e=1}^{n_{el}} \int_{\mathcal{S}_e \cup \mathcal{S}_d^{+,-}} \nabla_X N^i \cdot \boldsymbol{\sigma} \, dv \\ \mathbf{R}_I^{\text{coh}} &= \mathbf{A}_{e=1}^{n_{el}} \int_{\bar{\gamma}} \bar{N}^i \bar{\mathbf{t}}(\llbracket \boldsymbol{\varphi} \rrbracket) \, da \\ \mathbf{R}_I^{\text{ext}} &= \mathbf{A}_{e=1}^{n_{el}} \int_{\partial \mathcal{S}_{te}} N^i \mathbf{t}^p \, da \end{aligned} \tag{14}$$

Herein, the operator $\mathbf{A}_{e=1}^{n_{el}}$ denotes the assembly of all element contributions, i.e., the continuous and the discontinuous ones. By using an incremental iterative Newton–Raphson scheme to solve the non-linear set of Eq. (13) we arrive at the following linearized system of equations

$$\mathbf{R}_I^{k+1} = \mathbf{R}_I^k + d\mathbf{R}_I = \mathbf{0} \quad d\mathbf{R}_I = \sum_{J=1}^{n_{np}} \mathbf{K}_{IJ} d\boldsymbol{\varphi}_J \tag{15}$$

to be solved for the incremental update of the vector of unknowns $d\boldsymbol{\varphi}_J$. Here n_{np} is the number of global node points consisting of the standard nodes and the duplicated node points introduced in an elementwise fashion at the onset of crack propagation. Finally, we specify the incremental stiffness matrix

$$\mathbf{K}_{IJ} = \frac{\partial \mathbf{R}_I}{\partial \boldsymbol{\varphi}_J} = \mathbf{K}_{IJ}^{\text{int}} + \mathbf{K}_{IJ}^{\text{coh}} - \mathbf{K}_{IJ}^{\text{ext}} \tag{16}$$

in terms of its internal and cohesive contributions

$$\begin{aligned} \mathbf{K}_{IJ}^{\text{int}} &= \mathbf{A} \int_{e=1}^{n_{el}} \int_{S_e \cup S_d^{+,-}} \nabla_{\mathbf{x}} N^i \cdot \mathbf{e} \cdot \nabla_{\mathbf{x}} N^j \, dv \\ &\quad + \int_{S_e \cup S_d^{+,-}} \nabla_{\mathbf{x}} N^i \cdot \boldsymbol{\sigma} \cdot \nabla_{\mathbf{x}} N^j \, \mathbf{I} \, dv \\ \mathbf{K}_{IJ}^{\text{coh}} &= \mathbf{A} \int_{e=1}^{n_{el}} \int_{\tilde{\gamma}} \bar{N}^i \mathbf{T}_{\varphi} \bar{N}^j \, da + \int_{\tilde{\gamma}} \bar{N}^i \mathbf{T}_n \cdot \mathbf{G} \cdot \nabla_{\mathbf{x}} \bar{N}^j \, da \\ &\quad + \int_{\tilde{\gamma}} \bar{N}^i \bar{\mathbf{t}} \otimes [\mathbf{A} \cdot \nabla_{\mathbf{x}} \bar{N}^j] \, da \end{aligned} \tag{17}$$

by assuming that $\mathbf{K}_{IJ}^{\text{ext}} = \mathbf{0}$ vanishes identically. The fourth order tensor \mathbf{e} denotes the spatial elastic tangent moduli defined through the linearization of the Cauchy stress of equation (8.3) as

$$\mathbf{e} = \frac{1}{J} \lambda \mathbf{I} \otimes \mathbf{I} + \frac{1}{J} [2\mu - 2\lambda \ln(J)] \mathbf{i} \tag{18}$$

where \mathbf{i} is the fourth order identity tensor. With the constitutive definition of the cohesive tractions (9), we can further specify the incremental relation between tractions and discontinuities through the derivative of $\bar{\mathbf{t}}$ with respect to $[[\boldsymbol{\varphi}]]$ and $\bar{\mathbf{n}}$. These derivatives introduce the tangent operators \mathbf{T}_n and \mathbf{T}_{φ} ,

$$\mathbf{T}_{\varphi} = \frac{\partial \bar{\mathbf{t}}}{\partial [[\boldsymbol{\varphi}_n]]} \cdot [\bar{\mathbf{n}} \otimes \bar{\mathbf{n}}] + \frac{\partial \bar{\mathbf{t}}}{\partial [[\boldsymbol{\varphi}_m]]} \cdot [\mathbf{I} - \bar{\mathbf{n}} \otimes \bar{\mathbf{n}}] \tag{19}$$

$$\mathbf{T}_n = \left[\frac{\partial \bar{\mathbf{t}}}{\partial [[\boldsymbol{\varphi}_n]]} - \frac{\partial \bar{\mathbf{t}}}{\partial [[\boldsymbol{\varphi}_m]]} \right] \cdot [\bar{\mathbf{n}} \otimes [[\boldsymbol{\varphi}]] + [[[\boldsymbol{\varphi}]] \cdot \bar{\mathbf{n}}] \mathbf{I}]$$

whereby the derivatives with respect to $[[\boldsymbol{\varphi}_n]]$ and $[[\boldsymbol{\varphi}_m]]$ results in the following equations,

$$\frac{\partial \bar{\mathbf{t}}}{\partial [[\boldsymbol{\varphi}_n]]} = \frac{-f_t^2}{G_f} \exp\left(\frac{f_t}{G_f} [[\boldsymbol{\varphi}_n]] \cdot \bar{\mathbf{n}}\right) \bar{\mathbf{n}} \otimes \bar{\mathbf{n}} \tag{20}$$

$$\frac{\partial \bar{\mathbf{t}}}{\partial [[\boldsymbol{\varphi}_m]]} = d \mathbf{I}$$

see, e.g., Mergheim [17,20] for a detailed derivation of the above relations. Moreover, we have introduced the second order tensor $\mathbf{A} := [\mathbf{I} - \bar{\mathbf{n}} \otimes \bar{\mathbf{n}}] \cdot \bar{\mathbf{F}}^{-1}$ and the third order tensor $\mathbf{G} := -\bar{\mathbf{n}} \cdot [\mathbf{I} \otimes \bar{\mathbf{F}}^{-1}] + \bar{\mathbf{n}} \otimes \bar{\mathbf{n}} \otimes \bar{\mathbf{n}} \cdot \bar{\mathbf{F}}^{-1}$, the latter being the derivative of the normal vector $\bar{\mathbf{n}}$ with respect to the deformation gradient $\bar{\mathbf{F}}$. Herein \otimes denotes the non-standard

dyadic product according to the following componentwise representation $\mathbf{I} \otimes \bar{\mathbf{F}}^{-1} = \delta_{ik} F_{lj} \mathbf{e}_i \otimes \mathbf{e}_j \otimes \mathbf{e}_k \otimes \mathbf{e}_l$.

4 Implementation

For the spatial discretization, we suggest linear tetrahedral elements despite their well-known accuracy deficiencies. Linear elements allow an efficient implementation, especially for the integration over the fictitious discontinuity surface which, due to the use of linear interpolations, is typically assumed to be flat within each element. In what follows, we focus on the computational issues related to crack initiation, crack propagation and crack tracking.

4.1 Crack initiation

Throughout the computation, we impose the initial position of the crack by specifying the initial crack tip elements and the accurate crack position within the element. From there on, the current set of crack tip elements is computed and updated dynamically by checking the direct neighbors of the active crack tip elements. Accordingly, the current position of the crack tip is always known. Apparently, one of the most critical tasks during a crack propagation simulation is the determination of the direction in which the discontinuity is extending. To this end, we apply the principal stress based Rankine criterion for which a crack is initiated in an element as soon as the critical strength σ^{crit} is reached. Recall that the crack tip of a discontinuity is never located right at the integration point at which the Rankine criterion is evaluated because failing elements are always cut entirely at once. It is thus quite established in the literature to assume a smeared non-local process zone and apply the non-local stress $\bar{\boldsymbol{\sigma}}$ or related non-local strain variables as driving forces for crack initiation, see, e.g., [15,23] for size effects, [17,27,28] for two-dimensional problems and [8,9] for three-dimensional applications. Hence, we account for the non-local average stress in a sphere within radius r_{σ} around the crack tip. Typically, r_{σ} is chosen to be two to four times the characteristic element size $l_{el} = V_{el}^{1/3}$ with V_{el} being the entire element volume. We then denote the distance between the i th integration point and the discontinuity tip with r_i^{ip} . Furthermore we define V_{ip} the element volume related to the i th integration point and introduce the set \mathcal{I} of all integration points within the non-local averaging sphere.

$$\mathcal{I} = \left\{ i \in \{1, \dots, n^{\text{ip}}\} \mid r_i^{\text{ip}} < r_{\sigma} \right\} \tag{21}$$

Then we divide the set \mathcal{I} into two disjoint subsets $\mathcal{I} = \mathcal{I}^{\sigma} \cup \mathcal{I}^n$ where \mathcal{I}^{σ} contains the integration points of the uncracked elements and \mathcal{I}^n the integration points of the cracked elements in \mathcal{I} . Furthermore we define the total number of the respec-

tive subsets with $n^\sigma = \text{card}(\mathcal{I}^\sigma)$ and $n^n = \text{card}(\mathcal{I}^n)$. We then compute the non-local stress tensor $\tilde{\sigma}$ as

$$\tilde{\sigma} = \frac{1}{\sum_{j \in \mathcal{I}^\sigma} V_{ip}^j} \sum_{j \in \mathcal{I}^\sigma} V_{ip}^j \sigma_j \tag{22}$$

and solve its eigenvalue problem.

$$\tilde{\sigma} = \sum_{i=1}^3 \lambda_i^{\tilde{\sigma}} \mathbf{n}_i^{\tilde{\sigma}} \otimes \mathbf{n}_i^{\tilde{\sigma}} \tag{23}$$

We allow for crack propagation if the largest eigenvalue $\lambda_i^{\tilde{\sigma}_{\max}}$ exceeds the critical failure stress, i.e., $\lambda_i^{\tilde{\sigma}_{\max}} > \sigma^{\text{crit}}$. The eigenvector $\mathbf{n}_i^{\tilde{\sigma}_{\max}}$ related to this maximum eigenvalue defines the normal to the crack propagation direction $\tilde{\mathbf{n}} = \mathbf{n}_i^{\tilde{\sigma}_{\max}}$ in the spatial configuration. Following common practice in the literature, we limit the crack deviation angle α between two elements to avoid unphysical crack bifurcation and spurious turning of cracks. Technically speaking, we determine the new crack direction $\tilde{\mathbf{n}}$ according to the crack deviation angle condition

$$\tilde{\mathbf{n}} = \begin{cases} \mathbf{n}_i^{\tilde{\sigma}_{\max}} & \text{if } \alpha < \alpha^{\text{crit}} \\ \tilde{\mathbf{n}} & \text{if } \alpha \geq \alpha^{\text{crit}} \end{cases} \quad \text{with} \quad \cos(\alpha) = \tilde{\mathbf{n}} \cdot \mathbf{n}_i^{\tilde{\sigma}_{\max}} \tag{24}$$

where $\tilde{\mathbf{n}} = 1/n^n \sum_{i \in \mathcal{I}^n} \mathbf{n}_i$ is the average of all unit normal vectors of the existing crack surfaces in the sphere. The critical crack deviation angle α^{crit} is typically chosen to $\alpha^{\text{crit}} = \pi/6$ or $\alpha^{\text{crit}} = \pi/4$. Since we elaborate crack propagation in the reference configuration, we determine the material crack plane normal

$$\mathbf{N} = \tilde{\mathbf{J}}^{-1} \tilde{\mathbf{F}}^t \cdot \tilde{\mathbf{n}} \tag{25}$$

from the pull back of $\tilde{\mathbf{n}}$ via the deformation gradient $\tilde{\mathbf{F}}$.

4.2 Crack propagation

Once the direction of crack propagation is known from the evaluation of the failure criterion, an appropriate geometrical representation of the crack surface in three dimensions is needed. Since we apply a linear approximation of the deformation field the crack surface is represented by piecewise planar triangles and quadrilaterals in the reference configuration.

In a three-dimensional setting, the orientation of an element discontinuity is defined by its reference normal vector \mathbf{N} and a single point $\tilde{\mathbf{P}}$ to characterize the connection to the next element discontinuity. In contrast to two-dimensional problems where this point $\tilde{\mathbf{P}}$ is always uniquely defined this is not the case for three-dimensional problems, see Fig. 6. Therefore we follow [8] and define the new point $\tilde{\mathbf{P}} = 1/n^e \sum_i \mathbf{P}_i$ as the average of the pictured crack points \mathbf{P}_i ,

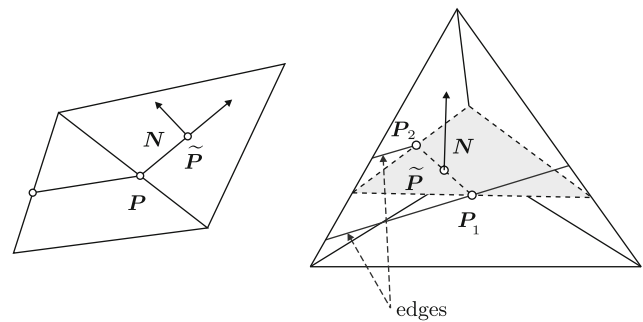


Fig. 6 Unique connecting point \mathbf{P} for the two-dimensional case and averaged connecting points \mathbf{P}_i depending on the adjacent cracked elements for the three-dimensional case

i.e. the midpoints of all adjacent cracked element edges $i = 1, \dots, n^e$.

4.3 Crack tracking

The application of non-locally averaged crack propagation criteria results in crack surfaces that are in general non-smooth. For practically relevant applications non-smooth failure surfaces are undesirable because of potential crack bifurcations for large crack deviation angles. Therefore we essentially need to identify powerful tracking algorithms to obtain a smooth representation of the crack surface. The main goal of this paper is to formulate and compare two fundamentally different local crack tracking methods and to elaborate their major advantages and disadvantages. Recall, however, that promising first attempts towards global crack surface representation have been presented recently in terms of global tracking algorithms [5, 14, 21, 22] or level set functions [10, 11, 26], see Gasser and Holzapfel [9] for an excellent overview of the algorithmic treatment of discontinuity surfaces in three dimensions.

4.3.1 Method I—the local Belytschko method

The following local tracking method was initially proposed by Areias and Belytschko [1]. It is based on a modification of the discontinuity direction depending on cracked neighboring elements. For this method we denote the intersection points of the existing edges from the cracked neighbor elements with \mathbf{C}_i . The number of cracked neighbor elements can vary between one and four, i.e., $i \in \{1, 2, 3, 4\}$, one edge is the minimum number and four is the maximum edge number for the case of a quadrilateral plane, compare the solid lines in Fig. 7. Furthermore this method introduces a unique labeling for the nodes, edges and faces of the tetrahedron. The six cases illustrated in Fig. 7 represent all possible configurations of the crack in the considered element. Case I only occurs during crack initiation, case II can either generate a

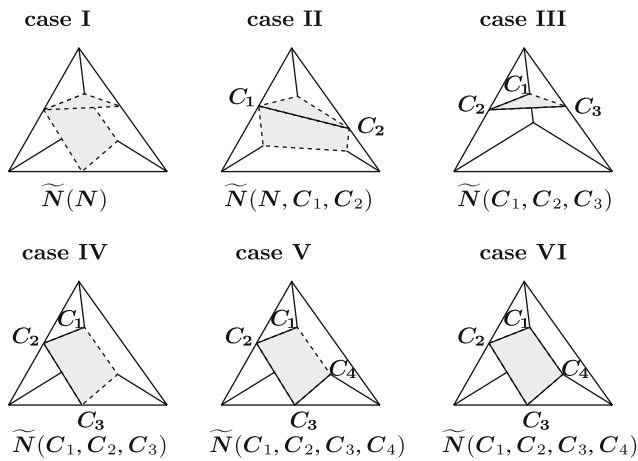


Fig. 7 Local tracking—Illustration of crack scenarios I–VI, corresponding crack neighbor points C_i and dependencies of crack plane normal \tilde{N} . Solid lines represent cracked neighbor elements whereas dashed lines depict possible potential crack configurations

triangular or a quadrilateral crack surface from one cracked neighbor element and cases III–VI are completely specified by the given intersection points of the cracked neighbors. The averaged crack plane normal \tilde{N} in the newly cracked element can then be calculated as follows

- o case I
 $\tilde{N} = N$
- o case II
$$\tilde{N} \propto N - \frac{N \cdot [C_1 - C_2]}{|C_1 - C_2|^2} [C_1 - C_2] \quad (26)$$
- o case III - VI
$$\tilde{N} = \frac{[C_1 - C_2] \times [C_3 - C_2]}{|[C_1 - C_2] \times [C_3 - C_2]|}$$

whereby N is the crack plane normal resulting from the eigenvalue problem as introduced in Sect. 4.1. The major drawback of this method is that it is extremely restrictive by construction since C_4 is required to lie in the C_1, C_2, C_3 plane. Provided this restriction is not violated, however, the algorithm generates perfectly smooth discontinuity surfaces at low computational cost. Note that during a standard crack propagation simulation cases II and III occur most frequently.

4.3.2 Method II—the non-local Holzapfel method

An alternative strategy that circumvents the above limitations has been introduced recently by Gasser and Holzapfel [9]. It essentially consists of two steps. The predictor step is applied to compute the normal vector N from the chosen failure criterion as suggested in Sect. 4.1 and the point \tilde{P} from the procedure described in Sect. 4.2. However, for many situations, the newly calculated element crack surface does not match the previously existing discontinuity. In many cases it is geometrically impossible to close a crack surface

if the element has been approached by cracks from different sides. Therefore a corrector step is introduced to close the existing crack surface as smoothly as possible. During the corrector step, the crack plane normal N is changed to the adapted normal \tilde{N} that accounts for additional information of the neighboring elements.

In general the existing crack surface is represented by n^{cr} nodes. These are the elementwise intersection points C_i of the element discontinuities and the element edges. As such, they represent elementwise the corners of the involved triangular or quadrilateral discontinuity plane as illustrated in Fig. 8. We assume that their position vectors C_i for $i = 1, \dots, n^{cr}$ are given relative to a global cartesian coordinate system $\{X, Y, Z\}$ with the orthonormal base vectors E_1, E_2, E_3 . We then introduce a sphere with the radius r_c around the center \tilde{P} of the currently analyzed element. Its radius r_c can just be chosen equivalent to the sphere’s radius r_σ from the computation of the average stress tensor but this is not imperative. Let us introduce the set of all intersection points C_i within this sphere

$$\mathcal{I}^c = \{i \in \{1, \dots, n^{cr}\} \mid r_i^{cr} < r_c\} \quad \text{with } n^c = \text{card}(\mathcal{I}^c) \quad (27)$$

where $r_i^{cr} = |C_i - \tilde{P}|$ obviously denotes the distance of the i th crack intersection point from the current element center \tilde{P} and n^c is the total number of points within the sphere.

The set of points \mathcal{I}^c is essential for the smoothing strategy. It forms a point cloud with the center C_c .

$$C_c = \frac{1}{n^c} \sum_{i \in \mathcal{I}^c} C_i \quad (28)$$

The orientation of this point cloud is given through a second cartesian coordinate system $\{\bar{X}, \bar{Y}, \bar{Z}\}$ which is characterized by a second set of orthonormal bases vectors $\bar{E}_1, \bar{E}_2, \bar{E}_3$. These orthonormal base vectors are the principal axes of the point cloud \mathcal{I}^c which are characterized in terms of the covari-

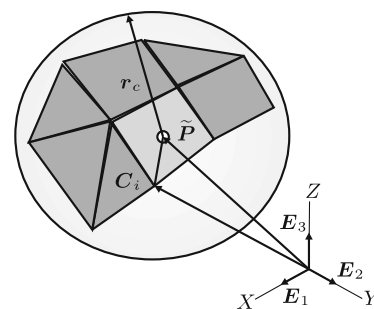


Fig. 8 Normal averaging sphere around the crack tip introducing the set \mathcal{I}^c of n^c crack intersection points within the sphere. Elementwise planar crack surface of triangles and quadrilaterals

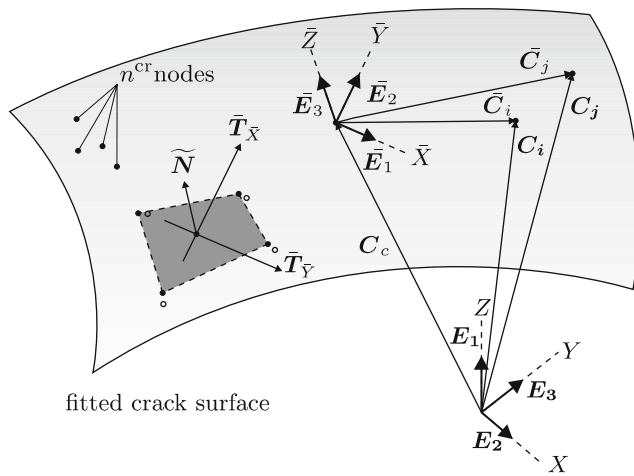


Fig. 9 Fitted three-dimensional crack surface

ance tensor Σ .

$$\Sigma = \sum_{i \in \mathcal{I}^c} [C_i - C_c] \otimes [C_i - C_c] \tag{29}$$

The set of base vectors $\bar{E}_1, \bar{E}_2, \bar{E}_3$ then follows straightforwardly from the corresponding eigenvalue problem

$$\Sigma = \sum_{i=1}^3 \lambda_i^\Sigma \bar{E}_i \otimes \bar{E}_i \tag{30}$$

Next we compute the corner points $\bar{C}_i = C_i - C_c$ related to the point C_c and transform the components of the corner points $[\bar{C}_i]$ from the global coordinate system $\{X, Y, Z\}$ to the local coordinate system $\{\bar{X}, \bar{Y}, \bar{Z}\}$ with the help of the orthogonal transformation tensor Q .

$$Q = \sum_{i=1}^3 \bar{E}_i \otimes E_i \tag{31}$$

The main idea of the corrector step is now to assume that the crack surface can be represented by either a linear or a quadratic function in the local coordinate system.

$$\bar{Z} = \begin{cases} a_0 + a_1 \bar{X} + a_2 \bar{Y} & \text{linear} \\ a_0 + a_1 \bar{X} + a_2 \bar{Y} + a_3 \bar{X}^2 + a_4 \bar{Y}^2 + a_5 \bar{X} \bar{Y} & \text{quadr} \end{cases} \tag{32}$$

The $j = 0, \dots, 5$ coefficients a_j in the local coordinate system follow from solving the corresponding least square's problem.

$$\Phi(a_j) = \sum_{i=1}^{n^{cr}} [\bar{Z}_i - \bar{Z}(a_j; \bar{X}_i, \bar{Y}_i)]^2 \rightarrow \min \tag{33}$$

Its solution introduces a symmetric system of linear equations for both cases, the linear and the quadratic approach.

$$\sum_{i=1}^{n^{cr}} \begin{bmatrix} 1 & \bar{X}_i & \bar{Y}_i & \bar{X}_i^2 & \bar{Y}_i^2 & \bar{X}_i \bar{Y}_i \\ \bar{X}_i^2 & \bar{X}_i \bar{Y}_i & \bar{X}_i^3 & \bar{X}_i \bar{Y}_i^2 & \bar{X}_i^2 \bar{Y}_i & \bar{X}_i^3 \bar{Y}_i \\ \bar{Y}_i^2 & \bar{X}_i^2 \bar{Y}_i & \bar{X}_i^4 & \bar{X}_i^2 \bar{Y}_i^2 & \bar{X}_i^3 \bar{Y}_i & \bar{X}_i^4 \bar{Y}_i \\ \bar{X}_i^4 & \bar{X}_i^3 \bar{Y}_i & \bar{X}_i^4 & \bar{X}_i^2 \bar{Y}_i^2 & \bar{X}_i^3 \bar{Y}_i & \bar{X}_i^4 \bar{Y}_i \\ \bar{Y}_i^2 & \bar{X}_i \bar{Y}_i^2 & \bar{X}_i^2 \bar{Y}_i^2 & \bar{X}_i \bar{Y}_i^3 & \bar{X}_i^2 \bar{Y}_i^3 & \bar{X}_i \bar{Y}_i^4 \\ \bar{X}_i \bar{Y}_i & \bar{X}_i^2 \bar{Y}_i & \bar{X}_i^3 \bar{Y}_i & \bar{X}_i^4 \bar{Y}_i & \bar{X}_i^5 \bar{Y}_i & \bar{X}_i^2 \bar{Y}_i^2 \end{bmatrix} \begin{bmatrix} a_0 \\ a_1 \\ a_2 \\ a_3 \\ a_4 \\ a_5 \end{bmatrix} = \sum_{i=1}^{n^{cr}} \begin{bmatrix} \bar{Z}_i \\ \bar{X}_i \bar{Z}_i \\ \bar{Y}_i \bar{Z}_i \\ \bar{X}_i^2 \bar{Z}_i \\ \bar{Y}_i^2 \bar{Z}_i \\ \bar{X}_i \bar{Y}_i \bar{Z}_i \end{bmatrix} \tag{34}$$

By construction, this element crack surface fits the existing corner nodes \bar{C}_i of the triangular and quadrilateral crack planes in a least-square sense. The coefficients a_j uniquely determine a smooth parametric representation of the crack surface and therefore we obtain the two tangent vectors $\bar{T}_{\bar{X}} = \bar{E}_1 + \frac{\partial \bar{Z}}{\partial \bar{X}} \bar{E}_3$ and $\bar{T}_{\bar{Y}} = \bar{E}_2 + \frac{\partial \bar{Z}}{\partial \bar{Y}} \bar{E}_3$ at an arbitrary point on the crack surface since \bar{Z} is always perpendicular to that surface. With these tangent vectors $\bar{T}_{\bar{X}}$ and $\bar{T}_{\bar{Y}}$, we compute the local representation of the crack plane normal \bar{N}

$$\bar{N} = \bar{T}_{\bar{X}} \times \bar{T}_{\bar{Y}} \tag{35}$$

and transform the components $[\bar{N}]$ to the global coordinate system. Note that in case of a linear surface description the normal vector \bar{N} is patchwise constant. In case of a quadratic surface description this vector would be evaluated at \bar{P} .

To complete this section we would like to point out two important facts. At first the corrector step can only be applied if a previous crack surface exist. Furthermore, this corrector step particularly violates the local failure criterion which is subject to the sphere's radius r_c . The radius r_c can be interpreted as a numerical weighting parameter between the geometry and the chosen failure criterion to overcome the difficulties with respect to the crack path tracking in three dimensions.

5 Examples

For practical applications it is of major interest whether the two proposed strategies are independent of the spatial discretization. The following numerical applications examine the two methods with respect to the load-displacement response, the resulting crack path surfaces and the smoothness of the resulting crack surfaces.

5.1 Rectangular block under tension

The first example consists of a simple mode I failure problem of a rectangular block subjected to a homogeneous tensile loading. The block has a square cross section of 1 mm² and a height of 2 mm. The block is fixed on the bottom and

loaded by a prescribed incremental displacement of 0.01 mm on its entire top, load case A, or on a single edge, load case B, see Fig. 10. For load case A, failure is initiated on both sides of the specimen, whereas for load case B failure is only initiated on the loaded side. The material parameters are chosen to $E=1000\text{N/mm}^2$, $\nu = 0.3$, $G_f = 100\text{N/mm}$, $f_t = 200\text{N/mm}^2$, $r_\sigma = 2l_{el}$, $r_n = 2l_{el}$. In order to compare the prescribed tracking strategies the computation is carried out with two different structured meshes, containing 4,410 and 10,501 elements.

First we discuss the results of load case A. As soon as the critical stress state is reached, the crack propagates through the specimen perpendicular to the loading direction. The complete separation of the block into two parts is slowed down by the cohesive tractions. The deformed configuration of the 10,501 element specimen analyzed with method I is shown in Fig. 12. As expected, the specimen exhibits unloading with an increasing crack opening. An initially elastic behavior can be observed before the critical stress value is reached and the load decreases exponentially with

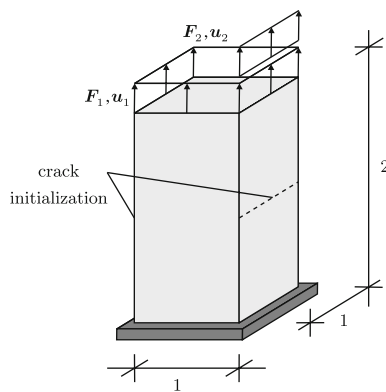


Fig. 10 Rectangular block under tension: Geometry and loading

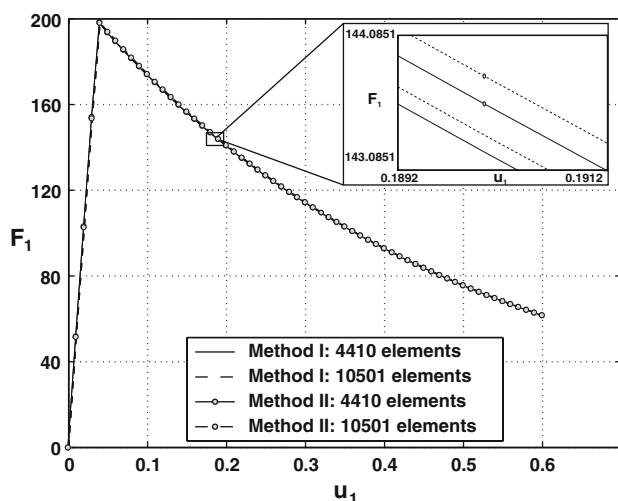


Fig. 11 Rectangular block under tension: Load-displacement relation for the different methods and load case A surface load

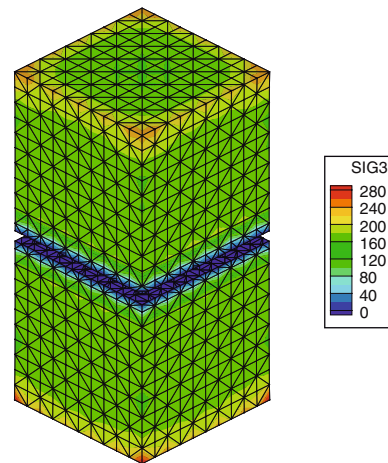


Fig. 12 Rectangular block under tension: Cauchy stress in loading direction for method I, load case A surface load, a displacement of 0.1mm and the discretization with 10501 elements

increased crack opening. This result is in good agreement with [19], where this example is computed with a prescribed crack plane normal. Obviously, the solutions are independent of the discretization and independent of the applied tracking method. Nevertheless, this equivalence holds only for the load-displacement relation and not for the smoothness of the crack surface. Here, the first method provides a smooth crack surface whereas the crack surface computed with method II displays jumps at the inter-element boundaries. Note that for the computation with method II, only a linear approximation of the crack surface has been applied.

Next we discuss the results for load case B which has been applied to initiate a curved crack surface. Note that for method II it is necessary that an initial crack surface exist when the algorithm starts. Accordingly, we fixed the crack plane normal N for the first row of initially cracked elements. For the sake of comparison, this crack initiation is applied for both methods. After the crack has propagated about two thirds of the block, the limit criterion of method I is met, i.e., the intersection points of the adjacent elements no longer lie within one plane, see the discussion in Sect. 4.3.1. This failure of method I was observed for both structured meshes.

We therefore turn to the analysis of method II, see Fig. 13, for the linear case of Eq. (32). Although this averaging approach promises to be more general, we encounter algorithmic difficulties as the crack is situated close to an element edge or face. Unlike the classical extended finite element method [1,2], the Hansbo method [12,13] we apply herein does not allow for discontinuities at element edges or faces. In detail the main problem occurs as the crack surface approaches the vicinity of a node and the jump at the element edge impedes the classification of this node with respect to the orientation of the node B^- and B^+ . Evidently, this essential drawback of the Hansbo method is even more likely to occur as the mesh is refined.

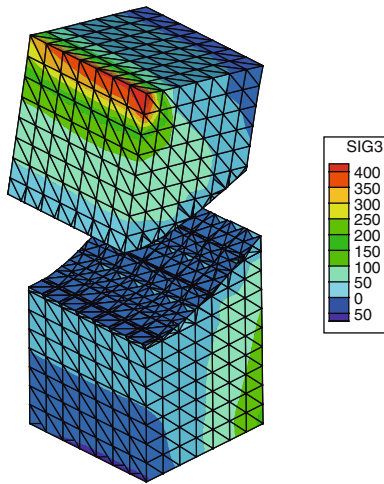


Fig. 13 Rectangular block under tension: Cauchy stress in loading direction for method II, load case B line load, a displacement of 0.6mm and the discretization with 4410 elements

5.2 Three point bending

The second example is the classical three point bending test. A simply supported beam is loaded by an imposed displacement at the center of its top, see Fig. 14. The material parameters are chosen to $E = 100 \text{ N/mm}^2$, $\nu = 0$, $G_f = 0.1 \text{ N/mm}$, $f_t = 1 \text{ N/mm}^2$, $r_\sigma = 3 l_{el}$, $r_n = 3 l_{el}$ and $\alpha = \sqrt{2}/2$. Furthermore, the crack shear stiffness is set to zero. Three different structured meshes with 8,400, 16,875 and 31,860 elements

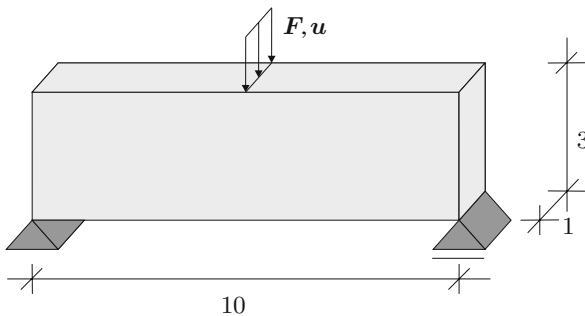


Fig. 14 Three point bending beam: Geometry and loading

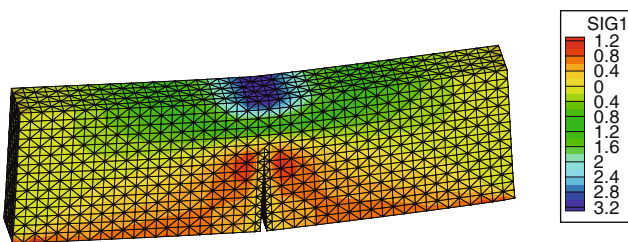


Fig. 15 Three point bending beam: Cauchy stress in loading direction for method II, a displacement of 0.25 mm and the discretization with 16,875 elements

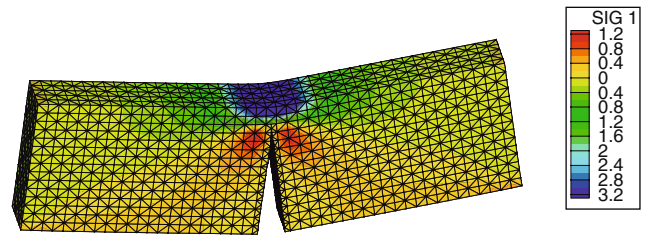


Fig. 16 Three point bending beam: Cauchy stress in loading direction for method II, a displacement of 0.5 mm and the discretization with 16,875 elements

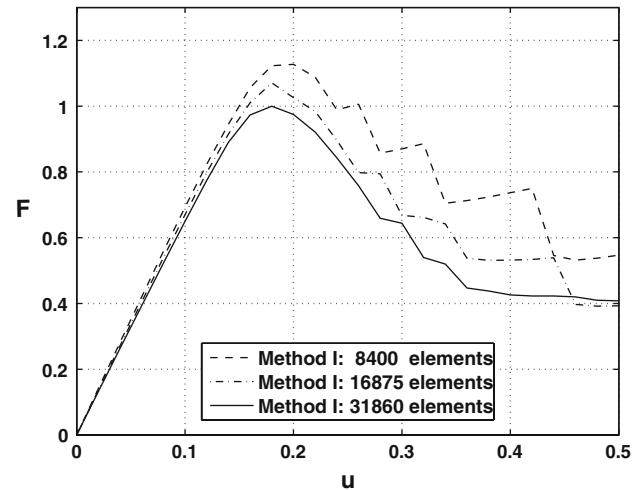


Fig. 17 Three point bending beam: Load-displacement relation for method I

are analyzed. Failure is initialized at the center of the lower face of the beam. As expected, due to the symmetric setup the crack path propagates straight upwards. Note that as the discontinuity propagates, we typically observe a change from mode I to mixed mode failure. To overcome this problem we choose the parameter α to $\alpha = \sqrt{2}/2$ and bound the crack deviation angle to 45° . Let us now further elaborate the load displacement response. Due to the proposed failure criterion which depends on the maximum tensile strength inside the elements and the parameter r_σ , the larger elements of the coarse mesh fail later. Accordingly, the peak load is slightly overestimated for the coarse discretization, see Figs. 17 and 18. Apart from this effect, the good agreement of the two load displacement curves confirms the objectivity of the method with respect to the discretization. A remarkably similar behavior is observed for both tracking strategies which are shown in Fig. 19. Furthermore, these results are in good agreement with the solutions of the three point bending beam analyzed in two dimensions, see e.g. [6,20,27]. Even though the resulting load displacement curves are nearly similar for the two different tracking strategies, the resulting crack surfaces show the same remarkable differences as the

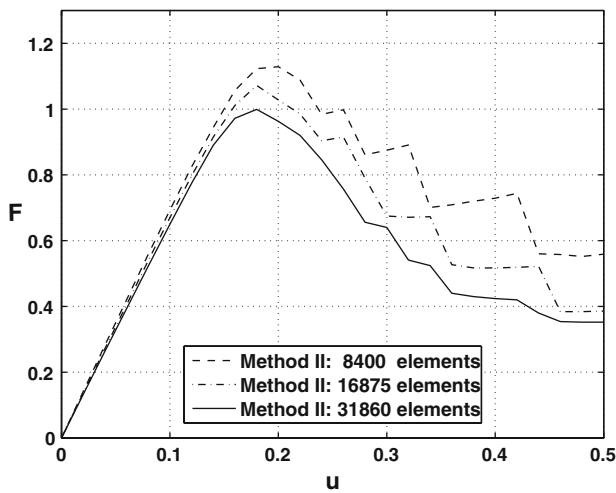


Fig. 18 Three point bending beam: Load-displacement relation for method II

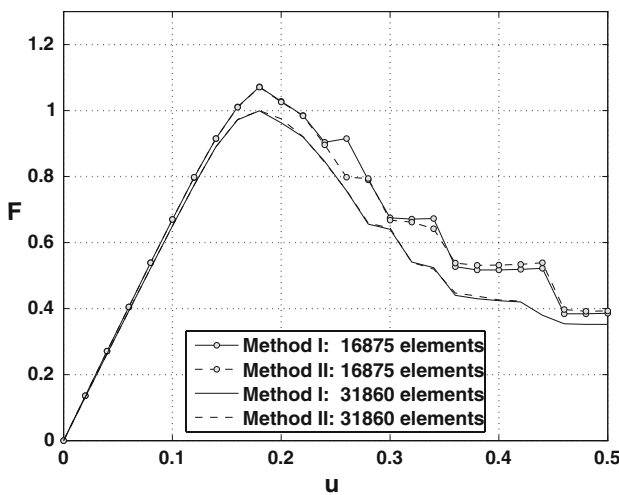


Fig. 19 Three point bending beam: Load-displacement relation for method I vs method II

first example. They are free of jumps for method I whereas small jumps at the inter-element boundaries are displayed for method II.

6 Discussion

Unlike two-dimensional crack simulations, three-dimensional simulations of discontinuities heavily rely on robust and efficient crack algorithms. While crack initiation criteria do not change significantly when increasing the number of spatial dimensions from two to three, crack tracking typically requires severe algorithmic reconsiderations related to a drastic increase of computational complexity and cost. In two dimensions, an elementwise linear crack is uniquely

determined in terms of one crack normal per element once an initial crack initiation point is given. In three dimensions, however, the representation of the crack is non-unique. The representation of choice can thus be understood as a compromise between a perfectly smooth crack surface which is usually too restrictive or rather too stiff from a mechanical point of view and a more flexible discontinuity which might exhibit jumps across the inter-element boundaries. In the present manuscript we provided a systematic comparison of representatives of both strategies, the smooth but stiff Belytschko method [1] and the flexible but non-smooth Holzapfel method [9]. Moreover, it was felt that it would be convenient to provide some implementational details and comments.

In summary, both methods have been shown capable to model planar cracks in three dimensions and simulate examples for which tracking algorithms are necessary. The Belytschko method was demonstrated to provide an entirely smooth crack surface. It is computationally cheap and extremely efficient since it requires only local modifications on the element level. However, unfortunately, it is inherently incapable of representing highly kinked or curved discontinuities. The Holzapfel method allows patchwise linear or quadratic representations of the crack. It requires global algorithmic modifications beyond the element level and eventually introduces inter-element jumps in the crack surface representation. In general, it is able to capture arbitrarily shaped crack surfaces in three dimensions.

Due to our particular discontinuity discretization based on the Hansbo method [12,13] rather than on the classical extended finite element method [1,2], our algorithm encounters algorithmic problems as soon as the crack surface approaches the vicinity of a node or edge. In the extended finite element method, these special cases are covered by a special treatment in the form of an enrichment of the particular node or edge. Unfortunately, a special enrichment of nodes or edges is not straightforward in the Hansbo method which exclusively introduces displacement degrees of freedom.

In general, it seems that for the simulation of highly kinked or curved discontinuities in three dimensions, a crack tracking method which essentially circumvents the particular deficiencies of the Hansbo method and at the same time allows for a perfectly smooth crack representation is highly desirable. The non-local Holzapfel method is a first step in this direction. Based on the systematic studies of this contribution, we conclude that a global crack tracking strategy as suggested e.g. by Chaves [5] and Oliver and Huespe [21] might be the ultimate solution of choice. Within this research project, we are currently elaborating the potential of global crack tracking strategies, see Jäger et al. [14]. The results which are indeed very promising will be presented in a follow up publication in the near future.

References

- Areias PMA, Belytschko T (2005) Analysis of three-dimensional crack initiation and propagation using the extended finite element method. *Int J Numer Meth Eng* 63(5):760–788
- Areias PMA, Belytschko T (2006) A comment on the article “A finite element method for the simulation of strong and weak discontinuities in solid mechanics” By A. Hansbo and P. Hansbo. [*Comput. Methods Appl. Mech. Engrg.* 193 (2004) 3523–3540]. *Comput Methods Appl Mech Eng* 195(9–12):1275–1276
- Dolbow J, Moës N, Belytschko T (2000) Discontinuous enrichment in finite elements with a partition of unity method. *Finite Elem. Anal. Design* 36(3–4):235–260
- Belytschko T, Moës M, Usui S, Parimi C (2001) Arbitrary discontinuities in finite elements. *Int J Numer Meth Eng* 50(4):993–1013
- Chaves EWV (2006) Tracking 3D Crack Path. Proceeding of the International Conference on Mathematical and Statistical Modeling in Honor of Enrique Castillo ICMSM. Ciudad Real, Spain
- de Borst R (2003) Numerical aspects of cohesive-zone models. *Eng Fract Mech* 70(14):1743–1757
- de Borst R, Guitiérrez MA, Wells GN, Remmers JC, Askes H (2004) Cohesive-zone models, higher-order continuum theories and reliability methods for computational failure analysis. *Int J Numer Meth Eng* 60(1):289–315
- Gasser TC, Holzzapfel GA (2005) Modeling 3D crack propagation in unreinforced concrete using PUFEM. *Comput Methods Appl Mech Eng* 194(25–26):2859–2896
- Gasser TC, Holzzapfel GA (2006) 3D Crack propagation in unreinforced concrete. A two-step algorithm for tracking 3D crack paths. *Comput Methods Appl Mech Eng* 195(37–40):5198–5219
- Moës N, Gravouil A, Belytschko T (2002) Non-planar 3D crack growth by the extended finite element and level sets - Part I: Mechanical model. *Int J Numer Meth Eng* 53(11):2549–2568
- Gravouil A, Moës N, Belytschko T (2002) Non-planar 3D crack growth by the extended finite element and level sets - Part II: Level set update. *Int J Numer Meth Eng* 53(11):2569–2586
- Hansbo A, Hansbo P (2004) A finite element method for the simulation of strong and weak discontinuities in solid mechanics. *Comput Methods Appl Mech Eng* 193(33–35):3532–3540
- Hansbo A, Hansbo P, Larson MG (2003) A finite element method on composite grids based on Nitsche’s method. *ESAIM: Math Model Numer Anal* 37(3):495–514
- Jäger P, Steinmann P, Kuhl E (2007) Modeling three-dimensional crack propagation. A comparison of crack path tracking strategies. (submitted for publication)
- Jirasek M, Rolshoven S, Grassl P (2004) Size effects on fracture energy induced by non-locality. *Int J Numer Anal Meth Geomech* 28(7–8):653–670
- Mergheim J, Kuhl E, Steinmann P (2004) A hybrid discontinuous Galerkin/interface method for the computational modelling of failure. *Commun Numer Meth Eng* 20(7):511–519
- Mergheim J, Kuhl E, Steinmann P (2005) A finite element method for the computational modelling of cohesive cracks. *Int J Numer Meth Eng* 63(2):276–289
- Mergheim J, Steinmann P (2006) A geometrically non-linear FE approach for the simulation of strong and weak discontinuities. *Comput Methods Appl Mech Eng* 195(37–40):5037–5052
- Mergheim J, Kuhl E, Steinmann P (2007) Towards the algorithmic treatment of 3D strong discontinuities. *Commun Numer Meth Eng* 23(2):97–108
- Mergheim J (2006) Computational Modeling of Strong and Weak Discontinuities. PhD thesis, Lehrstuhl für Technische Mechanik, TU Kaiserslautern
- Oliver J, Huespe AE (2002) On strategies for tracking strong discontinuities in computational failure mechanics. In: Mang HA, Rammendorfer FG, Erberhardsteiner J (eds) *Proceedings of the Fifth World Congress on Computational Mechanics (WCCM V)*. Austria, Vienna
- Oliver J, Huespe AE, Samaniego E, Chavez EVW (2004) Continuum approach to the numerical simulation of material failure in concrete. *Int J Numer Anal Meth Geomech* 28(7–8):609–632
- Patzak B, Jirasek M (2003) Process zone resolution by extended finite elements. *Eng Fract Mech* 70(7–8):957–977
- Remmers JJC, de Borst R, Needleman A (2003) A cohesive segments method for the simulation of crack growth. *Comput Mech* 31(1–2):69–77
- Sukumar N, Moës N, Moran B, Belytschko T (2006) Extended finite element method for three-dimensional crack modelling. *Int J Numer Meth Eng* 48(11):1549–1570
- Ventura G, Budyn E, Belytschko T (2003) Vector level sets for the description of propagating cracks in finite elements. *Int J Numer Meth Eng* 58(10):1571–1592
- Wells GN, Sluys LJ (2001) A new method for the modelling of cohesive cracks using finite elements. *Int J Numer Meth Eng* 50(12):2667–2682
- Wells GN, Sluys LJ, de Borst R (2002) Simulating the propagation of displacement discontinuities in a regularized strain-softening medium. *Int J Numer Meth Eng* 53(5):1235–1256